CFD investigation of Plate Channels

Masters Dissertation

by

Anton Johannesson

SUPERVISING PROFESSOR: CHRISTER FUREBY

MARCH 2022

Acknowledgements

This thesis draws an end to my five years of studying here at Lund University.

Firstly, I want to thank my supervising professor, Christer Fureby, for your assistance and mentorship during this project. Your knowledge and experience have guided me onto the right path when things have been stressful and unclear.

I want to thank my supervisor at Alfa Laval, Erik Engström, for your continuous support throughout the entire project and for always accompanying me at Alfa Laval. Your commitment made the project reach further than I expected.

I also want to thank my colleague, Gustav Karlsson, for sharing data from your own project and always being open for discussions when I have needed guidance in this project. The simulation you provided me with data from made it possible to analyse the GEKO-model from a completely different view.

Finally I want to thank all my colleagues at Alfa Laval, many of you have been part of this project and without your help, it would not have been the same. Your warm welcome in the difficult times of the pandemic has helped me stay motivated and positive.

Thank you!

Anton Johannesson
2022-03-31, Lund

Abstract

Alfa Laval has a wide product range for plate heat exchangers that can be applied in most industries. The constant development of new and old heat exchangers drive the need for new and efficient methods that can reliably be used in the development process. In this thesis, a new turbulence model within a computational fluid dynamics-program has been tested and evaluated for one of Alfa Lavals commercial plate heat exchangers to see if better results can be achieved compared to older models.

This project has been divided into three main parts. Firstly, a mesh-study was conducted for a typical heat exchanger geometry in order to understand mesh-size in relation to interesting parameters. Secondly, since the turbulence-model has a set of parameters for tuning the flow, an initial parameter study was conducted. Testing combinations of the parameters on a smaller geometry. This was also combined with a high-resolved large eddy simulation (LES) to study the parameters effect on local phenomenons. Lastly, a global parameter-study was conducted for the commercial plate heat exchanger.

The project showed that better accuracy can be achieved with certain sets of model-parameters depending on different plate-combinations. Future work is however needed as it could be interesting to further study local phenomenons using a LES-model on a plate heat exchanger that has experimental data, but most importantly test the GEKO-model for more heat exchangers.

Contents

1   Introduction

1.1   Alfa Laval

Alfa Laval is a world leading company at the front edge of three technologies, heat transfer, separation and fluid handling. These three key technologies are applicable in almost any industry. Alfa Laval is divided into three business divisions, Energy Environment, Food & Water and Marine industry which in total generate a net sale of 41.47B SEK while being active in over 100 countries worldwide. [6]

1.2   Background, Purpose & Objectives

Alfa Laval run lots of Computational Fluid Dynamics simulations yearly on their existing product lines of Plate Heat Exchangers (PHE). These are usually limited to traditional Reynolds Averaged Navier-Stokes (RANS) turbulence models due to computational limitations. All heat exchangers are tested extensively on different rigs in their lab. However experimental data and simulations does not correlate as expected and new methods with increased accuracy would greatly benefit future development.

As of January 2019, ANSYS have developed a new RANS turbulence model called the Generalized k-ω model (GEKO-model). The purpose of the model is to allow modifications for different flow scenarios without tampering with the calibration for basic flows (such as simple flow over a plate or flow over backward facing step). This is something new that have not been possible before with conventional RANS turbulence models, making this model more adjustable and applicable for many different flow scenarios.[4]

The purpose of this thesis is therefore to calibrate the GEKO model for a commercial plate heat exchanger in order to validate if the model results correlate better with experiments compared to the more traditional turbulence models.

2 Theory

2.1 Heat Exchangers

There are a wide variety of heat exchangers designed for different applications. However all of them have the same working principle, to transfer heat between two or more fluid medias at different temperatures. An illustration of a very simple heat exchanger can be seen in figure 1 below.
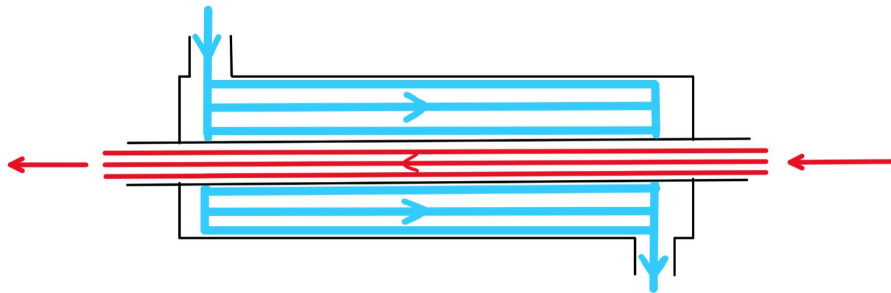

Figure 1: *Heat exchanger illustrating cold (blue) and warm (red) liquid passing and exchanging heat.*

2.2 The Gasketed Plate Heat Exchanger

The gasketed heat exchanger is a plate heat exchanger that utilizes gaskets for sealing channels where fluids flow and exchange heat between the individual plates. It is the largest product group at Alfa Laval within the Energy Environment Division whilst delivering products for the Marine and Food Water Division as well. [1]

The plates are sealed by pressing the plates and gaskets together using a frame (fixed cover) and a pressure plate (movable cover), see figure 2.The plates are hanging from the carrying bar and positioned correctly in the bottom by the guide bar. The complete assembly can be seen in figure 2 below. Figure 2 also illustrates how the fluids are transported within the heat exchanger thus exchanging heat. The flow direction is also displayed, where in this case the the heat exchanger run the fluid medias counter current. This is the most common flow direction in a plate heat exchanger however, co-current can be advantageous for high viscosity fluid medias. It also shows how the gasket hinders the two fluids from direct contact.
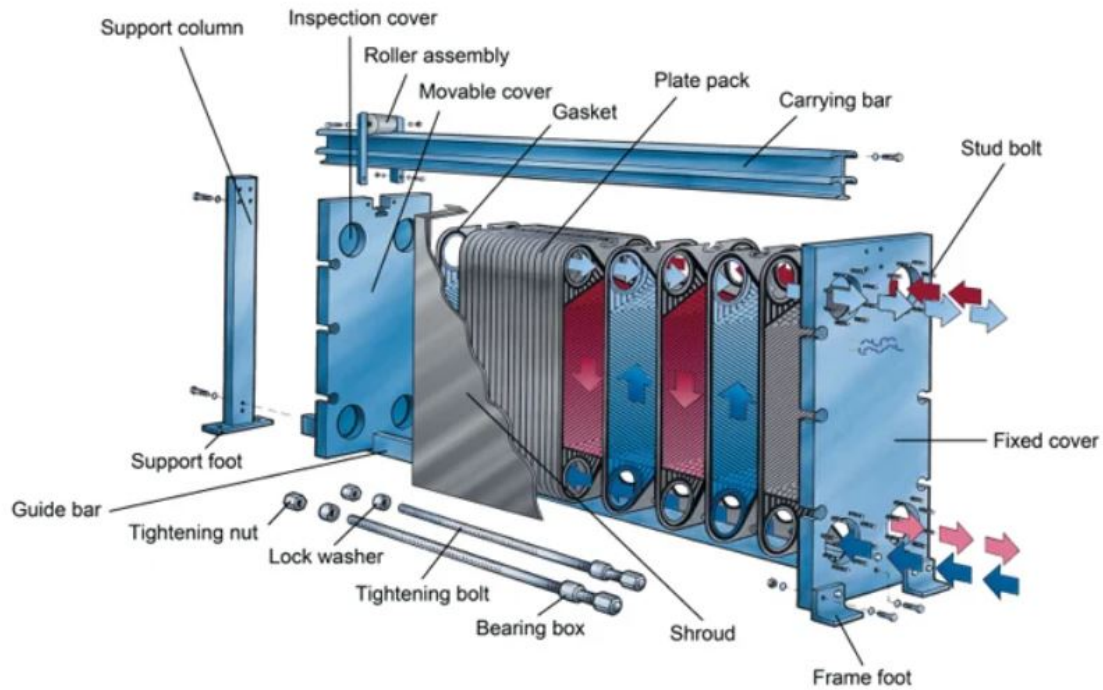
Figure 2: *An exploded view of a typical Gasketed Plate Heat Exchanger.* [7]

This design enables for disassembling when cleaning or maintenance is needed. It also allows for changing capacity by easily removing or adding plates.

2.2.1 The Plate

Figure 3 shows how a general plate with the sealing gasket can look like in a Gasketed Plate heat Exchanger. The plates are stacked so that every other plate has the gasket positioned like the figure and the others are mirrored, creating channels where the fluids can flow.
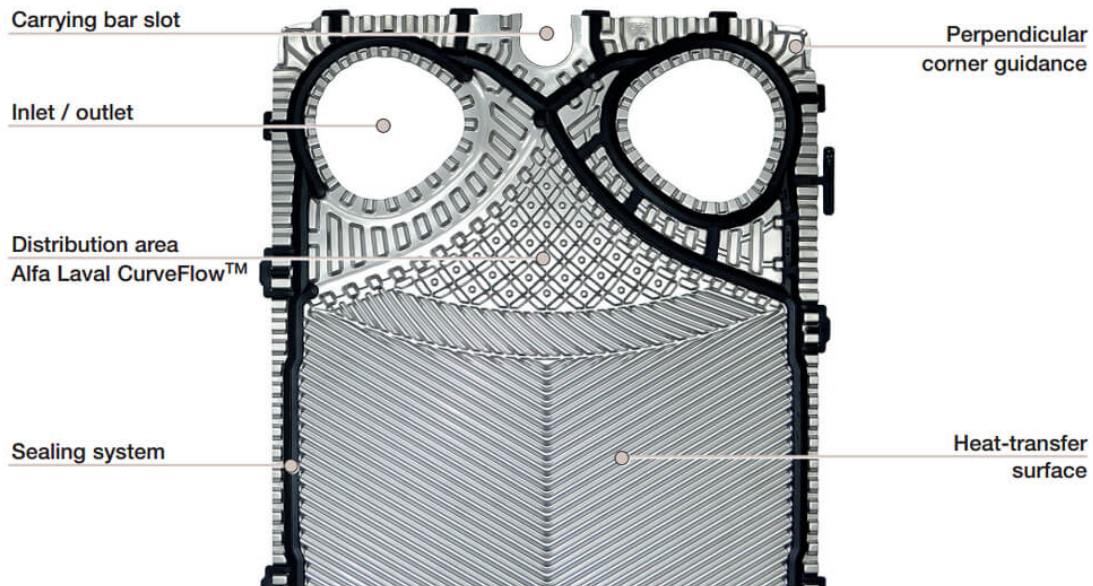
Figure 3: *A typical plate in a Gasketed Plate Heat Exchanger.[9]*

Focusing more on the channel itself, it can be divided into three parts. The port where the inlet/outlet is placed, the distribution area and the heat transfer area. Even though all parts are vital for the function of the heat exchanger, the heat transfer area is the most important. It has a pattern known as the herringbone pattern and is shown in the lower part of figure 3. The angle of the corrugated pattern is called the chevron angle and can be varied for different applications.

2.2.2 Channel types

There are multiple different plates for a general gasketed plate heat exchanger since both pressing depth and the chevron angle can be varied. For this thesis, only the two chevron angles have been tested. These are named the L- and H-plate and can be seen in figure 4.

Figure 4: *The two different chevron angles in the plates.[9]*

Low theta stands for a small chevron angle illustrated in the left of figure 4.The fluid flows down (or up) the plate which results in less turbulence since the fluid follows the grooves more easily. This also results in lower heat transfer but lower pressure drop when being used for a channel in the heat exchanger. High theta yields more turbulence and heat transfer but increases the pressure drop due to increased flow resistance.

Since one channel consists of two plates, a total of three combinations can be created. One channel with two L-plates called the L-channel, one with two H-plates called the H-channel and a channel using one H-plate and one L-plate called the M-channel, see figure 5. As explained before, the L-channel has less pressure drop and heat transfer while the H-channel has the highest. The M-channel is somewhere between the L- and H-channel. This allows for many different combinations and gives a large application-range for the products.
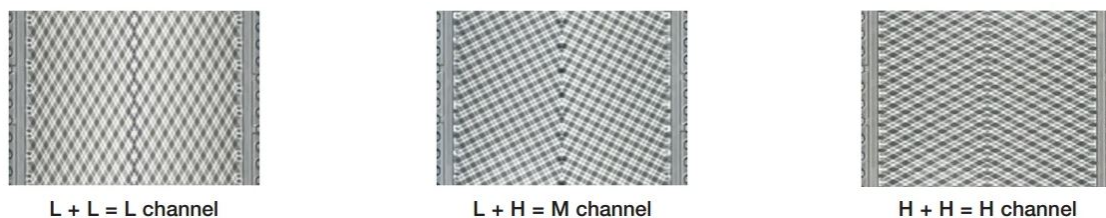

Figure 5: *The three different channels created by the L- and H-plates. [9]*

2.3   Thermodynamic relations for Heat Exchangers

When comparing performance in heat exchangers, the values of interest is most often, pressure drop and heat transfer. The most common equation that holds for a heat

exchanger is equation (1).

$$P = (kA)\text{LMTD} \tag{1}$$

Where P is the rate of heat transfer (heat load), k the overall heat transfer coefficient, A the heat transfer area and $LMTD$ the logarithmic mean temperature difference defined by equation (2).

$$\text{LMTD} = \frac{\Delta T_1 - \Delta T_2}{ln\frac{\Delta T_1}{\Delta T_2}} \tag{2}$$

In a counter current flow direction configuration $\Delta T_1 = T_1 - T_4$ and $\Delta T_2 = T_2 - T_3$. T_1 is the temperature in at the hot side, T_2 is the temperature out at the hot side. T_3 is the temperature in at the cold side, T_4 is the temperature out at the cold side. [8]

Since the temperature difference between the two sides vary nonlinearly between the inlet and outlets, an logarithmic mean temperature difference accounts is used instead. It is used for determination of the temperature driving force for the system and a higher number effectively results in higher overall heat transfer in the system.[3]

In equation (1) the heat load is unknown and most often, the quantity kA is sought. The heat load can then be computed by the use of equation (3), using either channel-side.

$$P = \dot{m}c_p\Delta T \tag{3}$$

The overall heat transfer coefficient for a thin wide plate is defined in equation (4).

$$\frac{1}{k} = \frac{1}{\alpha_1} + \frac{1}{\alpha_2} + \frac{\delta}{\lambda} \tag{4}$$

Where α_1 and α_2 are the convective heat transfer coefficients for each channel sides, δ the wall thickness and λ the thermal conductivity of the material between the fluids.[8]

2.4 Reynolds Number

The Reynolds number is a dimensionless parameter that is often used when describing flow characteristics. The Reynolds Number for channel flow is defined in equation (5).

$$\text{Re} = \frac{\rho u D_H}{\mu} \tag{5}$$

Where ρ is the fluid density, u the reference velocity, D_H is the hydraulic diameter and μ the dynamic viscosity.

The hydraulic diameter and the velocity-massflow relationship is defined as:

$$D_h = \frac{4A}{l} \tag{6}$$

$$\dot{m} = \rho u A \tag{7}$$

$A = sw$ is the cross-sectional area of the channel where s is the press depth of the plate and w the channel width. l is the circumference of the cross-sectional area ($l = 2s + 2w$). equation (5) can be rewritten under the assumption that $w >> s$ using equation (6) and equation (7) into:

$$\mathrm{Re}_{PHE} = \frac{2\dot{m}}{\mu w} \tag{8}$$

The Reynolds number is most often used when comparing different flows with each other by using the *Reynolds-number similarity*. This means that if the flow cases compared are similar geometrically and have the same Reynolds Number, the flows are considered dynamically similar. [10]

2.5 Governing Equations

It is of interest to describe fluid motion using the governing equations applied on a finite fluid element fixed in space. This is called the Eulerian approach. The fluid element is seen as a continuum and therefore molecular motions or structures are ignored. The three conservation laws of physics are stated below:

- The fluid mass is conserved.

- The rate of change in momentum equals the forces acting on a fluid element.

- The rate of change in energy for a element is equal to the heat rate added and the rate of work done.

The three conservation laws are translated into, the continuity-, momentum- and energy-equations. These are shown in equation (9),equation (10) and equation (11).

$$\frac{\partial \rho}{\partial t} + \frac{\partial (\rho u_i)}{\partial x_j} = 0 \tag{9}$$

$$\frac{D(\rho u_i)}{Dt} = \frac{\partial \tau_{ij}}{\partial x_j} - \frac{\partial p}{\partial x_i} + S_{Mi} \tag{10}$$

$$\frac{D(\rho e)}{Dt} = -\frac{\partial q_i}{\partial x_i} + u_i \frac{\partial (p)}{\partial x_i} + \frac{\partial}{\partial x_j}(u_i \tau_{ij}) + S_E \tag{11}$$

Where u_i is the velocity vector, ρ the fluid density, τ_{ij} is the surface stress tensor acting on the fluid element, p is the pressure, S_{Mi} is a source vector for the momentum equation, E the energy for the fluid element, q_i the heat flux and S_E a source vector for the energy-equation. $\frac{D}{Dt}$ is the material derivative defined for u_i as $\frac{Du_i}{Dt} = \frac{\partial u_i}{\partial t} + u_j \frac{\partial u_i}{\partial x_j}$

Chosen heat transfer fluid media for this project is water and since velocities are well below Ma=0.3, where Ma is the Mach number equation (9)-equation (11) can be modified under the assumption of incompressiblity and a Newtonian fluid, body-forces are also neglected. The resulting equation (12)-equation (13) are called the Navier-Stokes Equations for an in-compressible Newtonian fluid.

$$\frac{\partial u_i}{\partial x_j} = 0 \tag{12}$$

$$\rho \left(\frac{\partial u_i}{\partial t} + u_j \frac{\partial u_i}{\partial x_j} \right) = -\frac{\partial p}{\partial x_i} + \mu \frac{\partial^2 u_i}{\partial x_j \partial x_j} \tag{13}$$

$$\rho \left(\frac{\partial e}{\partial t} + u_j \frac{\partial e}{\partial x_j} \right) + u_j \frac{\partial p}{\partial x_j} + p \frac{\partial u_j}{\partial x_j} = \frac{\partial}{\partial x_j} \left(k \frac{\partial T}{\partial x_j} \right) + \frac{\partial}{\partial x_j}(u_i \tau_{ij}) \tag{14}$$

2.6 The finite volume discretization

The Navier-Stokes equations have no analytical solution for general flow cases. It can only be solved numerically by implementing a discretised grid, applying boundary conditions and initial conditions. ANSYS Fluent is using a method called the finite volume discretization with cell center storage in the commercial CFD code.[5]

Consider the Navier-Stokes equations equation (12)-equation (13). For simplicity only the momentum equation will be discretised in this section.

Firstly, the equation is integrated over a computational cell with the volume V.

$$\iiint_{CV} \left[\rho \left(\frac{\partial u_i}{\partial t} + u_j \frac{\partial u_i}{\partial x_j} \right) \right] \partial V = \iiint_{CV} \left[-\frac{\partial p}{\partial x_i} + \mu \frac{\partial^2 u_i}{\partial x_j \partial x_j} \right] \partial V \tag{15}$$

All terms can be integrated individually.

$$\iiint_{CV} \rho \frac{\partial u_i}{\partial t} \partial V + \iiint_{CV} \rho u_j \frac{\partial u_i}{\partial x_j} \partial V = -\iiint_{CV} \frac{\partial p}{\partial x_i} \partial V + \iiint_{CV} \mu \frac{\partial^2 u_i}{\partial x_j \partial x_j} \partial V \qquad (16)$$

The divergence theorem is implemented

$$\rho \frac{\partial u_i}{\partial t} V + \oiint_A \rho u_i u_j n_j \partial A = -\oiint_A p n_i \partial A + \oiint_A \mu \frac{\partial u_i}{\partial x_j} n_j \partial A \qquad (17)$$

The flux over a face is assumed to be constant, hence the area integrals can be rewritten into summations over an arbitrary polyhedra cell with a number of faces M, using the Green Gauss Theorem.[12]

$$\rho \frac{\partial u_i}{\partial t} V + \sum_{i=1}^{M} \rho u_{fi} u_{fi} n_{fi} A_i = -\sum_{i=1}^{M} p n_{fi} A_i + \sum_{i=1}^{M} \mu \frac{\partial u_{fi}}{\partial x_{fi}} n_{fi} A_i \qquad (18)$$

Quantities indexed fi are face values for the given quantity. Due to all data being saved in the cell centers, some sort of interpolation to obtain the face values are needed. These methods are described in section 2.7 below.

2.7   Discretisation schemes

Since all discrete values are stored in the cell center, some sort of interpolation is needed for both the convection, pressure and diffusion terms in the example relating to equation (18). There are many different methods of interpolating face values. This section aims to describe the most common schemes available and used in the analysis. In ANSYS Fluent, the discretisation scheme for the convective and pressure term is selectable for the user, while the diffusion term always uses the central differencing scheme. [5]

In order to illustrate the reasoning and calculations, figure 6 will be used. W stands for west and E for east relating to the node of interest P. Face values are typed in lowercase letters. For illustrative reasons, no other surrounding cells are shown in the two other directions, but can be used in a similar manner as referred to below. The distance between the cell centers is assumed to be δx.
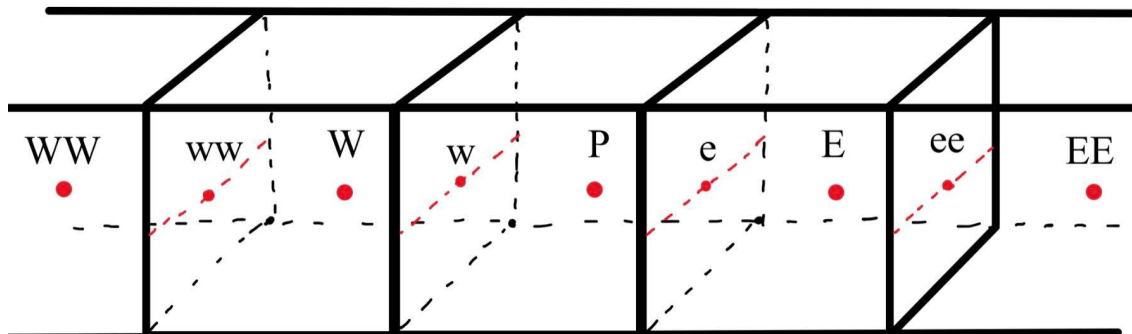
Figure 6: *Quadrilateral elements with neighbour nodes and faces.*

2.7.1 Upwind Scheme

One of the most simple schemes is the upwind scheme. Its a first order scheme from a first order Taylor series expansion around node P. It only transport values and information in the flow direction. It assumes that the cell value is an averaged value constant through the cell. The face values are therefore set to the value of the upstream cell center. This means that for the velocity u with a flow direction from west to east in figure 6 relating to equation (18), $u_e = u_P$ and $u_w = u_W$.

Due to its simplicity, the upwind scheme has been widely used in early CFD simulations. However, its main drawback is that it creates whats known as false diffusion if applied to flows which doesn't follow the grid lines. This have been found to sometimes generate physically wrong results and is therefore not recommended for accurate flow calculations.[12][12]

2.7.2 Linear Upwind Scheme

Like the Upwind scheme, the linear upwind scheme is also a Taylor series expansion around node P but of second order. In this scheme the gradient for the upstream cell multiplied by the displacement vector from the upstream cell centroid to the face centroid has been added. Like its precursor, the linear upwind scheme is dependent on the flow direction. [12]

14

On a general form, it can be written:

$$u_f = u + \nabla u \cdot \overline{r} \tag{19}$$

But for the case in figure 6:

$$u_w = u_P + \frac{\partial u}{\partial x} * \frac{\delta x}{2} = u_P + \frac{u_P - u_W}{\delta x} \frac{\delta x}{2} = \frac{3}{2} u_P - \frac{1}{2} u_W \tag{20}$$

2.7.3 Central Differencing Scheme

The traditional central differencing scheme uses neighbouring cell values to linearly calculate the face values according to:

$$u_e = \frac{u_E + u_P}{2} \qquad or \qquad u_w = \frac{u_W + u_P}{2} \tag{21}$$

In ANSYS commercial code, apart from cell center values, the gradients are also recreated and multiplied with the direction vectors from the cell center to the face centroid. 0 and 1 refers to the cells sharing the face.

$$u_f = \frac{1}{2}(u_0 + u_1) + \frac{1}{2}(\nabla u_0 \cdot \overline{r_0} + \nabla u_1 \cdot \overline{r_1}) \tag{22}$$

Unlike the upwind schemes, the central differencing scheme does not consider flow direction for the cell face values. This can for some cases make the solutions unstable due to problem with the transportiveness of the scheme. [12]

2.7.4 Other Schemes

Apart from the schemes described above, there exists a lot of others schemes which are both of higher order or just constructed differently. However, for this report, the schemes mentioned above are sufficient to give the reader an understanding for face-value interpolation schemes and those used in this project.

2.8 Boundary layer

A very important part of CFD is the treatment of walls. For the majority of simulations, the goal is to understand how an object, or in this case a pattern, interacts with the flow. Since for most cases a no-slip condition is applied at a boundary, $u_{y=0} = 0$, large

gradients appear along the walls. These gradients are responsible for the majority of turbulence created in the domain and can have a major impact on the overall flow characteristics. The flow is also affected by viscous damping of velocities perpendicular to the wall and the normal fluctuations are reduced in the near-wall region. Therefore boundary-layers need careful treatment and can have a significant impact on generated results if done wrong. [11]

A turbulent boundary layer can be categorised by three main parts. The viscous sub-layer, the buffer-layer and the log-layer. These are generally discussed in terms of how much influence viscous forces have on the described flow. In the viscous sub-layer the viscous forces are dominant and are decreasing through the buffer-layer to the log-layer.[10]

When discussing the different layers and mesh size, no absolute metric is used. Instead, the non-dimensional parameters u^+ and y^+ is used which are defined in equation (23) and equation (24) below.

$$y^+ = \frac{\rho u_\tau y}{\mu} \tag{23}$$

$$u^+ = \frac{\overline{u}}{u_\tau} \tag{24}$$

Where u_τ is the friction velocity defined by:

$$u_\tau = \sqrt{\frac{\tau_w}{\rho}} \tag{25}$$

Where τ_w is the wall shear stress, y is the wall-normal distance to the wall.

It has been shown that in the viscous sub-layer ($y^+ < 5$), the relation between the non-dimensional velocity u^+ and wall distance $y+$ is linear, $u^+ = y^+$. For the log-layer, these quantities have the following relation: $u^+ = \frac{1}{\kappa}\ln(y^+) + B$ where $\kappa = 0.41$ is the Von-Kármáns constant and B is a constant approximated to 5.2. For the buffer-layer, none of these relationships hold up. Instead in this layer the viscous dominant linear relationship transitions to the log-law.[10]

It is therefore important when choosing wall treatment, that the viscous dominant region is either resolved or is represented in what is called a wall model. The different functions are displayed in figure 7 below.

16
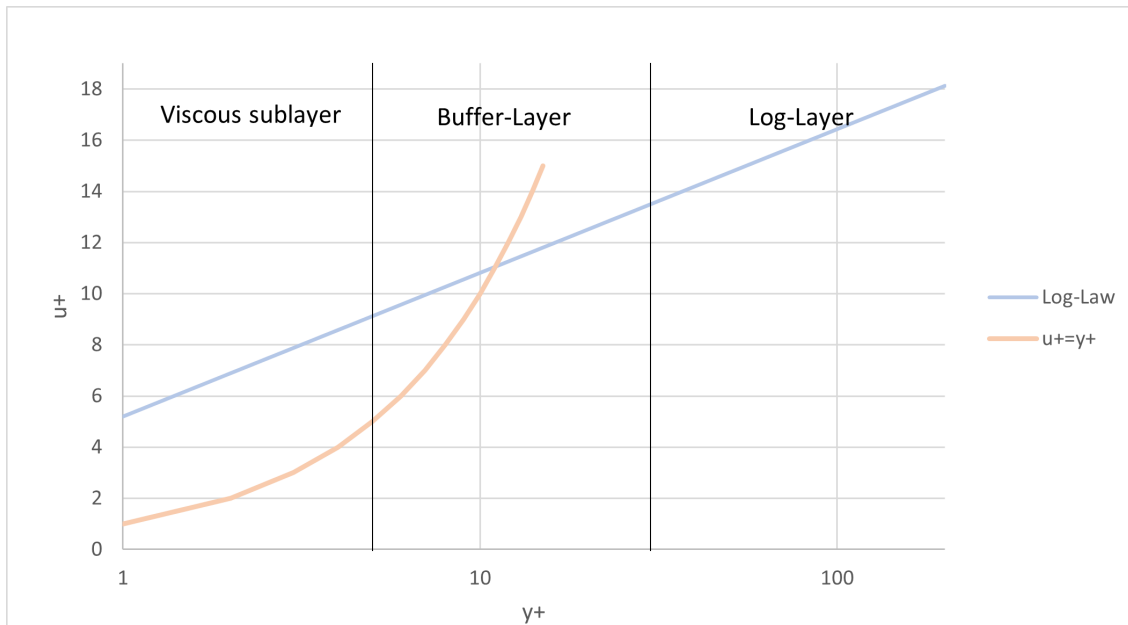
Figure 7: *The near-wall non-dimensional velocity u^+ shown as a function of y^+*

2.8.1 Wall treatment

From the previous section, the need for extra treatment of walls are clear. In industrial CFD-programs there are mainly two different types of treatment, near wall treatment and wall functions.

For a near wall treatment, the entire boundary layer is resolved from the viscous sub-layer to the free stream. This can be a very computational demanding task and is most often only used for simulations were flow separation is present or the near wall region is of interest.[12]

The other option is to use so-called wall functions. Instead of having a refined mesh along the boundary. The first cell is located with its boundary in the log-layer. By doing this, the viscous affected inner layers can be bypassed and an semi-empiric formula can be implemented, recreating a gradient for the surface. This is more computational efficient due to the reduced cell-count but are usually only applicable for high Reynolds's numbers.[12]

2.8.2 First layer thickness estimation

To get an approximation for a desired $y+ = 1$ in the first simulations the following calculation was carried out in order to set a reasonable first layer thickness. This was just conducted for the first simulation. Later on the first layer thickness was analysed in section 5.1

Equation (23) was rewritten as following:

$$y^+ = \frac{\rho u_\tau y}{\mu} \longrightarrow y = \frac{\mu y^+}{\rho u_\tau} \tag{26}$$

Where the skin friction velocity is defined by equation (25) and τ_w is the wall shear stress and is calculated as:

$$\tau_w = \frac{1}{2} c_f \rho u^2 \tag{27}$$

Where the skin friction coefficient for internal flow for a circular tube with a smooth surface is derived from empiric relations as: $c_f = 0.079 \mathrm{Re}^{-0.25}$

2.9 Turbulence modeling

A big part in computational fluid dynamics is how the turbulence of the flow is modeled. There are many different ways in means of computational capacity and complexity where direct numerical simulations are the most costly but simple in terms of no modeling needed. The 2-equation models are the cheapest however more complex since they require a lot of modeling and assumptions being made. It should be noted that there exists models using less equations (one and zero-equation models). However these often have geometrical limitations. Therefore will only the three different methods DNS, LES and RANS be presented.

2.9.1 Direct Numerical Simulation

The purpose of direct numerical simulation is to resolve all time- and length-scales so that no turbulence modeling is needed. Therefore the governing Navier-Stokes equations are solved directly without the assumption of any turbulence modelling. Since all length scales need to be resolved, an extremely fine mesh is required. Also a very fine time-step is needed in order capture the small scale turbulence motions. As expected, this is extremely costly computational wise and even the most simple flow cases require

supercomputers to be computed. On the other hand this method is superior in terms of accuracy as no dissipation of energy is being modeled and all sizes of flow structures are being resolved. Almost all computational power is spent on the smaller scales.[10]

2.9.2 Large Eddy Simulation

The purpose of Large Eddy Simulation is to resolve large unsteady eddys that might appear in the flow while the smaller scales is modelled. Since most computational capacity in DNS simulation is spent on smaller scales. By modelling these, the general unsteady flow structures such as vortex shedding or unsteady separation can be kept while saving capacity.

This is done by applying a filter that separates the velocity vector into one resolved, time dependent vector and one filtered, that requires modelling. The resolved field is solved similarly to an DNS simulation by solving the Navier-Stokes equations while the filtered field is modelled similarly to section 2.9.3 below. This is still a very computational costly method and can require fine spatial and time discretisations. [10]

2.9.3 Reynolds-Averaged Navier-Stokes Simulations

The most common way to simulate flows in the industry is by running RANS-simulations which utilises the Reynolds-Averaged Navier-Stokes equations. This method is a lot less costly computational wise, but require a lot of modelling and assumptions. The time dependency is removed by averaging the Navier-Stokes equations according to Reynolds Decomposition lessening the amount of iterations needed for a well resolved solution.

In order to obtain the RANS-equations, the Reynolds decomposition must be introduced to the Navier-Stokes equations, equation (12)-equation (13).The Reynolds decomposition states that the velocity field can be described by a mean and fluctuating part, equation (28).

$$u = \overline{u} + u' \tag{28}$$

The RANS-equations can then be obtained by inserting equation (28) in equation (12) and equation (13) followed by time-averaging or ensemble-averaging. Time-averaging is

an average taken over a specific time-interval while an ensemble-average is an average of a multiple of samples at a specific time. Both are similar if the the system is statistically stationary.[13]

The Reynolds-Averaged Navier-Stokes equations are presented in equation (29) & equation (30).

$$\frac{\partial \overline{u_i}}{\partial x_j} = 0 \tag{29}$$

$$\rho \left(\frac{\partial \overline{u_i}}{\partial t} + u_j \frac{\partial \overline{u_i}}{\partial x_j} \right) = -\frac{\partial \overline{p}}{\partial x_i} + \mu \frac{\partial^2 \overline{u_i}}{\partial x_j \partial x_j} - \frac{\partial}{\partial x_j} \left(\overline{u_i' u_j'} \right) \tag{30}$$

Here it can be seen that there is an additional term added in the momentum equation. This is called the Reynolds Stress tensor and introduces six new variables. Since there are only four equations and ten variables now, there is some modelling needed. This is often named the *closure problem* and is where turbulence modelling is needed.[10]

In turbulence modelling the Reynolds Stress Tensor is often put in relation to the mean flow, thus eliminating the fluctuating parts of the velocities. There are many different ways of modelling the Reynolds Stress Tensor, the most common way to model it is by introducing the eddy viscosity.

2.9.4 Eddy Viscosity

The Eddy viscosity hypothesis states that the Reynolds Stresses are coupled to the mean rate of strain tensor and is given by equation (31)

$$\overline{u_i' u_j'} = \frac{2}{3} k \delta_{ij} - \frac{\mu_T}{\rho} \left(\frac{\partial \overline{u_i}}{\partial x_j} + \frac{\partial \overline{u_j}}{\partial x_i} \right) \tag{31}$$

Where δ_{ij} is the Kronecker's delta defined as $\delta_{ij} = 1$ if $i = j$ and $\delta_{ij} = 0$ if $i \neq j$.

Hence, now there is only a need to determine the eddy viscosity for the system of equations to be closed. This can be done in a number of different ways. But usually the most basic form of the eddy viscosity is described as a multiplication of a velocity and a length.

$$\nu_T = u^* l^* \tag{32}$$

The two introduced quantities can be determined in different ways. Most commonly

they are related to the turbulent kinetic energy. Most focus will lie on two equation models for determining the eddy viscosity. These will be further discussed in the next section. It is however worth mentioning that there exists algebraic and one equation models as well. These are not very often used for other than simple shear flows as they require input in regards to the geometry. Thus making them not so applicable for the majority of different cases.

2.9.5 Two equation turbulence models

There are many different two-equation turbulence models, however the most common ones are the k-epsilon and k-omega models. The model analysed in this thesis is a modified version of the k-omega model that will be presented later.

The k-epsilon model

The standard k-epsilon model is the most common turbulence model available in commercial CFD codes. It was developed in the early 1970s, where W.P Jones and B.E Launder were credited with developing the Standard k-epsilon model.

The Standard k-epsilon turbulence model is built upon introducing two transport equations equation (33) & equation (34) for both k, turbulent kinetic energy and ε, dissipation rate. These two quantities are then used to compute the eddy viscosity, equation (35)

$$\frac{\partial(\rho k)}{\partial t} + u_i \frac{\partial(\rho k)}{\partial x_i} = P_k - \rho\varepsilon + \frac{\partial}{\partial x_j}\left[\frac{\mu_t}{\sigma_k}\frac{\partial k}{\partial x_j}\right] \tag{33}$$

$$\frac{\partial(\rho\varepsilon)}{\partial t} + u_i \frac{\partial(\rho\varepsilon)}{\partial x_i} = C_{1\varepsilon}\frac{\varepsilon}{k}P_k - C_{2\varepsilon}\rho\frac{\varepsilon^2}{k} + \frac{\partial}{\partial x_j}\left[\frac{\mu_t}{\sigma_\varepsilon}\frac{\partial\varepsilon}{\partial x_j}\right] \tag{34}$$

$$\mu_t = \rho C_\mu \frac{k^2}{\varepsilon} \tag{35}$$

Where $P_k = 2\mu_t S_{ij}S_{ij}$ is the production of turbulent kinetic energy and $S_{ij} = \frac{1}{2}\left(\frac{\partial u_i}{\partial x_j} + \frac{\partial u_j}{\partial x_i}\right)$ is the mean rate of strain tensor.

The k-omega model

The k-omega model is similar in its' equation for the transport of k and the calculation of μ_t to the k-epsilon model. However the second equation for ε differs and a new quantity

$\omega = \frac{\varepsilon}{C_\mu k}$ is introduced. In a similar way to equation (33)-equation (35), the transport equations for the k-omega model are shown below.

$$\frac{\partial(\rho k)}{\partial t} + u_i\frac{\partial(\rho k)}{\partial x_i} = P_k - \rho\beta^* k\omega + \frac{\partial}{\partial x_j}\left[\frac{\mu_t}{\sigma_k}\frac{\partial k}{\partial x_j}\right] \tag{36}$$

$$\frac{\partial(\rho\omega)}{\partial t} + u_i\frac{\partial(\rho\omega)}{\partial x_i} = \frac{\alpha\omega}{k}P_k - \beta\rho\omega^2 + \frac{\partial}{\partial x_j}\left[\frac{\mu_t}{\sigma_\omega}\frac{\partial\omega}{\partial x_j}\right] + \frac{\rho\sigma_d}{\omega}\frac{\partial k}{\partial x_j}\frac{\partial\omega}{\partial x_j} \tag{37}$$

$$\mu_t = \frac{\rho k}{\omega} \tag{38}$$

The k-omega SST model

The k-omega SST model is a blend between the standard k-epsilon and standard k-omega model. It accurately handles adverse pressure gradients from the k-omega model and is stable in the free stream from the k-epsilon model. The models are combined using a blending function F1 in the term $\frac{\rho\sigma_d}{\omega}\frac{\partial k}{\partial x_j}\frac{\partial\omega}{\partial x_j}$ which is the term separating the models. The transport equations for the k-omega SST model is shown in equation (39)-equation (40) below.

$$\frac{\partial(\rho k)}{\partial t} + u_i\frac{\partial(\rho k)}{\partial x_i} = P_k - \rho\beta^* k\omega + \frac{\partial}{\partial x_j}\left[\frac{\mu_t}{\sigma_k}\frac{\partial k}{\partial x_j}\right] \tag{39}$$

$$\frac{\partial(\rho\omega)}{\partial t} + u_i\frac{\partial(\rho\omega)}{\partial x_i} = \frac{\gamma}{\nu_T}P_k - \beta\rho\omega^2 + \frac{\partial}{\partial x_j}\left[\frac{\mu_t}{\sigma_\omega}\frac{\partial\omega}{\partial x_j}\right] + 2(1-F_1)\frac{\rho\sigma_d}{\omega}\frac{\partial k}{\partial x_j}\frac{\partial\omega}{\partial x_j} \tag{40}$$

Where

$$\mu_T = \frac{\rho a_1 k}{max(a_1\omega, \Omega F_2)} \tag{41}$$

$$F_1 = tanh(arg_1^4) \tag{42}$$

$$arg_1 = min\left[max\left(\frac{\sqrt{k}}{\beta^*\omega d}\right), \frac{4\rho\sigma_{\omega 2}k}{CD_{k\omega}d^2}\right] \tag{43}$$

$$CD_{k\omega} = max(2\rho\sigma_{\omega 2}\frac{1}{\omega}\frac{\partial k}{\partial x_j}\frac{\partial\omega}{\partial x_j}, 10^{-20}) \tag{44}$$

$$F_2 = tanh(arg_2^2) \tag{45}$$

$$arg_2 = max\left(2\frac{\sqrt{k}}{\beta^*\omega d}, \frac{500\nu}{d^2\omega}\right) \qquad (46)$$

The Generalized k-omega model (GEKO)

The Generalized k-omega model is a new turbulence model based on the formulation for the k-omega model. It was developed with the intention of consolidating traditional models by allowing the user to adjust six free parameters without tampering with the basic calibration of the model. The six parameters C_{SEP}, C_{NW}, C_{JET}, C_{MIX}, $C_{CCORNER}$ and C_{CURV} are described individually below.

- C_{SEP}, affects the sensitivity of boundary layer separation. By increasing C_{SEP} the eddy viscosity is reduced, effectively making the model more sensitive for separation .

- C_{NW}, acts only within the boundary layer. By increasing C_{NW} the wall shear stress and wall heat transfer increases.

- C_{JET}, ables the user to adjust spreading rates of jets. By increasing C_{JET} the spreading rate for jets decreases. C_{JET} is applied in a sub-model for C_{MIX} and has no effect if $C_{MIX} = 0$.

- C_{MIX}, acts in the free flow and ables the user to adjust spreading rates of free shear flows. By increasing C_{MIX} the spreading rate for free shear flow increases. In order to obtain optimal values for the spreading rate when varying C_{SEP}, an correlation for C_{MIX} exists that maintains optimal free shear flows.

- C_{CORNER}, can be used for activating a nonlinear stress-strain term taking secondary flows into account.

- C_{CURV}, ables the user to activate a curvature correction term already implemented for other models. Increasing C_{CURV} should more accurately capture strong curvatures.

The six parameters are implemented through the functions F_1, F_2 and F_3 in the transport equation for dissipation rate, see equation (48).

$$\frac{\partial(\rho k)}{\partial t} + u_i\frac{\partial(\rho k)}{\partial x_i} = P_k - \rho\beta^* k\omega + \frac{\partial}{\partial x_j}\left[\frac{\mu_t}{\sigma_k}\frac{\partial k}{\partial x_j}\right] \qquad (47)$$

23

$$\frac{\partial(\rho\omega)}{\partial t} + u_i\frac{\partial(\rho\omega)}{\partial x_i} = C_{\omega 1}F_1\frac{\omega}{k}P_k - C - \omega 2F_2\rho\omega^2 + \rho F_3 CD + \frac{\partial}{\partial x_j}\left[\frac{\mu_t}{\sigma_\omega}\frac{\partial\omega}{\partial x_j}\right] \tag{48}$$

Where

$$\mu_T = \rho\frac{k}{max(\omega, \frac{S}{C_{Realize}})} \tag{49}$$

$$P_k = -\tau_{ij}\frac{\partial u_i}{\partial x_j} \tag{50}$$

$$\tau_{ij}^{EV} = -\rho\overline{u_i'u_j'} = \mu_t 2S_{ij} - \frac{2}{3}\rho k\delta_{ij} \tag{51}$$

$$CD = \frac{2}{\sigma_{ij}}\frac{1}{\omega}\frac{\partial k}{\partial x_j}\frac{\partial\omega}{\partial x_j} \tag{52}$$

$$\tau_{ij} = \tau_{ij}^{EV} - C_{CORNER}\frac{1.2\mu_t}{max(0.3\omega, \sqrt{0.5(S^2 - \Omega^2)})}(S_{ik}\Omega_{kj} - \Omega_{ik}S_{kj}) \tag{53}$$

With

$$S_{ij} = \frac{1}{2}\left(\frac{\partial u_i}{\partial x_j} + \frac{\partial u_j}{\partial x_j}\right) \qquad \Omega_{ij} = \frac{1}{2}\left(\frac{\partial u_i}{\partial x_j} + \frac{\partial u_j}{\partial x_j}\right) \tag{54}$$

and

$$S = \sqrt{2S_{ij}S_{ij}} \qquad \Omega = \sqrt{2\Omega_{ij}\Omega_{ij}} \tag{55}$$

3   Set-up

In this section physical assumptions, numerical methods and limitations will be presented.

3.1   Geometry Description

3.1.1   Test plate

The test plate used in the initial part of the thesis can be seen in figure 8. It uses rectangular inlet and outlets and has high-theta patterned plates closing the channel, described in section 2.2.2. This geometry has lots of simplifications compared to a commercial heat-exchanger and is only used for research purposes.
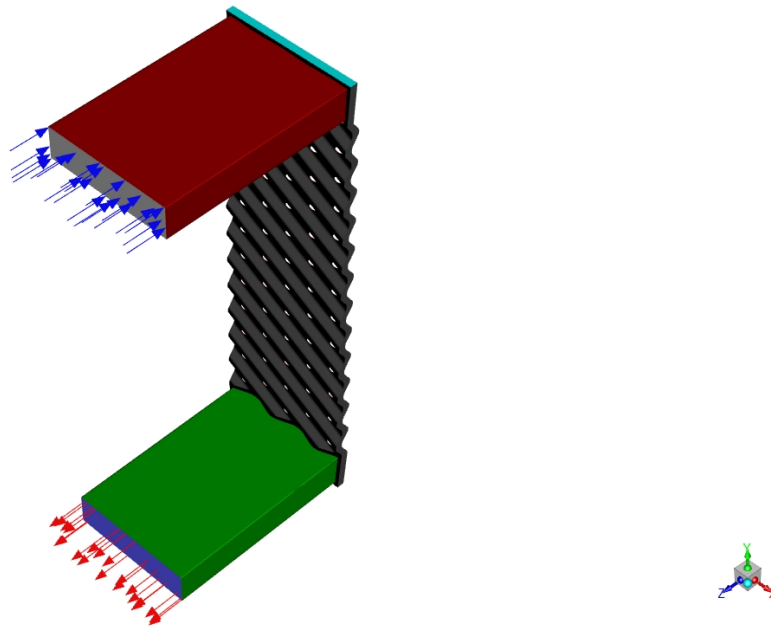
Figure 8: *The test channel used in the initial part of the thesis.*

3.1.2   Commercial plate

The commercial plate is approximately 30% larger then the test plate. Therefore no ports are being simulated and the inlet is directly into the channel. The main difference compared to the test plate is the distribution area that is between the chevron pattern and the ports. These distribute the fluid across the plate since the ports are a lot smaller

then the width of the plate. The channel created from the commercial plate is shown in figure 9.
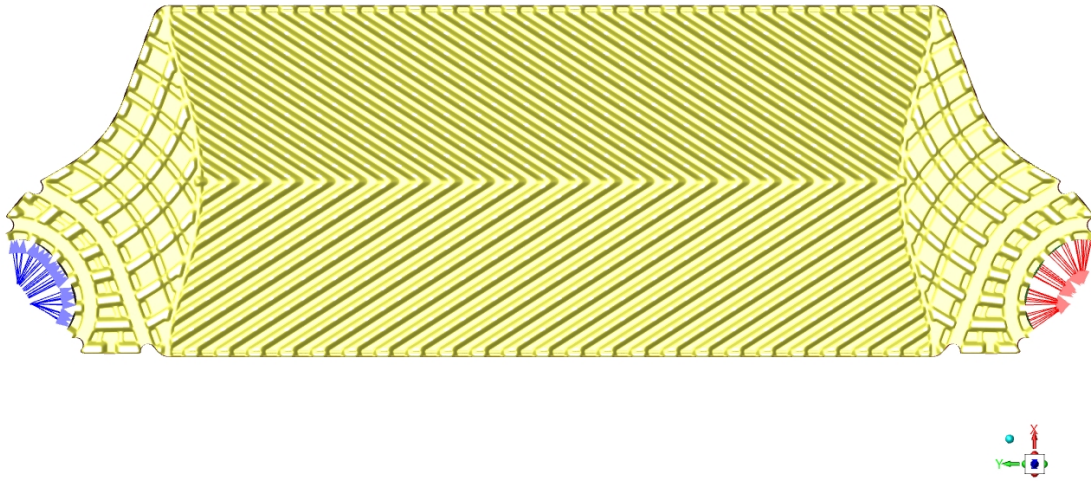
Figure 9: *The commercial plate used in the final part of the thesis.*

3.2   Boundary Conditions

3.2.1   Test channel

For the test channel a fixed velocity was set at the inlet in accordance with the desired Reynolds number at the rectangular port with a temperature of 20 °C. The outlet was defined as a pressure outlet with a gauge pressure of 0Pa on the other port, see figure 8. On all other walls, a no-slip condition is used.

How initial conditions for turbulent kinetic energy and dissipation are determined are not directly specified in the user manual for ANSYS Fluent. They are however based on the turbulence intensity:

$$I \equiv \frac{u'}{\overline{u}} \tag{56}$$

Based on this, the turbulent kinetic energy and dissipation can then be determined:

$$k = \frac{3}{2}(\overline{u}I)^2 \tag{57}$$

$$\omega = \frac{\rho k}{\mu} \left(\frac{\mu_t}{\mu} \right)^{-1} \tag{58}$$

Due to the complex flow domain and generally high turbulence within the heat exchanger, a value of 5% was set.[2]

This geometry was run for three Reynolds numbers, 1600, 2000 and 5000. For the RE 1600 case, a convection heat transfer boundary condition was assigned to the side with no ports on the chevron pattern. The convection coefficient was set to $20000\frac{W}{m^2 K}$ and the reference temperature 60°C. For RE2000 and RE5000 both sides of the chevron pattern has a convective boundary condition with a coefficient set to $20000\frac{W}{m^2 K}$ and a reference temperature of 80°C

3.2.2 Commercial channel

For the commercial plate the inlet was set as a pressure inlet where three total pressures was set and an inlet temperature of 30°C. This type of boundary condition was used in order to get a more accurate massflow distribution over the inlet surface. The outlet is defined as a pressure outlet. Turbulent kinetic energy and dissipation are set in accordance with section 3.2.1

For the commercial plate, a heat transfer boundary condition was set with corresponding convective heat transfer coefficients to the different plate combinations defined in table 1 below. Reference temperature was set to 50 °C.

Table 1: Convective heat transfer coefficients for plate pattern	
Plate pattern	$\alpha \left[\frac{W}{m^2 K} \right]$
Low theta	31200
High theta	46000
Mix theta	63500

3.3 Constraints and Assumptions

3.3.1 Geometry/Mesh Constraints

One significant constraint in this model is that only one channel is simulated. Therefore, the convection heat transfer coefficient set is constant over the entire surface which in real life would vary due to temperature changes on both sides.

Since only one channel is simulated, port effects are overlooked as well as effects from other openings from previous and later channels. This is something that has not been

studied thoroughly, but might have a big impact on some plate combinations.

Another constraint in the program used is that heat transfer was applied on the entire plate marked in yellow, see figure 9. This is not correct since no exchange of heat occurs in the region where the gasket groove is situated. Therefore, a surface was created on the edge of the gasket grooves and temperatures were mass-averaged over these surfaces in order to only capture heat transfer in the correct region.

3.3.2 Physical Models

The fluid media used in this project is water. The water is modelled as in-compressible Newtonian fluid whos' properties are temperature dependent. The test-plate simulations for the Re 1600 case are run temperature independent in order to compare to another PhD project running parallel to this project.

Regarding heat transfer, no conjugated heat transfer will be simulated due to computational capacity limitations. Instead of comparing to the experiments made on the commercial plate, comparisons were made with Alfa Lavals empirical correlations which are derived from experiments. The other channel that is not simulated was modelled to have approximately a constantly high heat transfer coefficient. By doing this the heat transfer is solely based on the cold simulated side since α_1 will be dominant in deciding the heat transfer coefficient based on equation (4).

The convection heat boundary condition was applied straight on the fluid face instead of modelling the thermal resistance in the plate. This in order for simplification but could easily be removed in the comparative thermal relations for the plate by increasing the thermal conductivity of it.

3.3.3 Numerical Methods

For spatial discretisation the user can choose the discretisation scheme for the pressure, momentum, turbulent kinetic energy, specific dissipation rate and energy.

For pressure a second order central differencing scheme is used explained in section 2.7.

Lastly for the momentum, turbulent kinetic energy, specific dissipation rate and energy a second order upwind scheme is used. Higher order schemes are available but it was chosen for this thesis that schemes of second order would be sufficient.

4   Methodology

This project can be divided into three parts. In the first part a short literature study was conducted on the papers regarding the GEKO turbulence model as well as familiarizing with the CFD program ANSYS Fluent and the geometries that would later be used in the project.

For the second part of the project a mesh convergence study was conducted in order to find a suitable mesh that is balanced between computational capacity and gives consistent results.

The third part of the project was to analyse the GEKO-model and test different parameter combinations in order to calibrate the model to the commercial heat exchanger. The results were then summarized and concluded.

Since this plate is very large the initial mesh-study and parameter analysis was made on the smaller test plate. This smaller plate is used in a PhD project where both advanced LES and one DNS simulation have been performed, which some of the results has been incorporated.

5 Results & Discussion

5.1 Mesh convergence study

A mesh convergence study was conducted in order to understand the dependence on cell size compared to the results given from the simulation. This was run on a smaller test-plate with similar Reynolds numbers as the commercial plate. To find an acceptable mesh size that would yield accurate results while being computationally efficient, three different mesh sizes were run with the standard parameters for the GEKO model. Heat transfer in form of average outlet temperature and pressure drop was globally analyzed while locally, the velocities were analyzed in a line probe shown in figure 10.
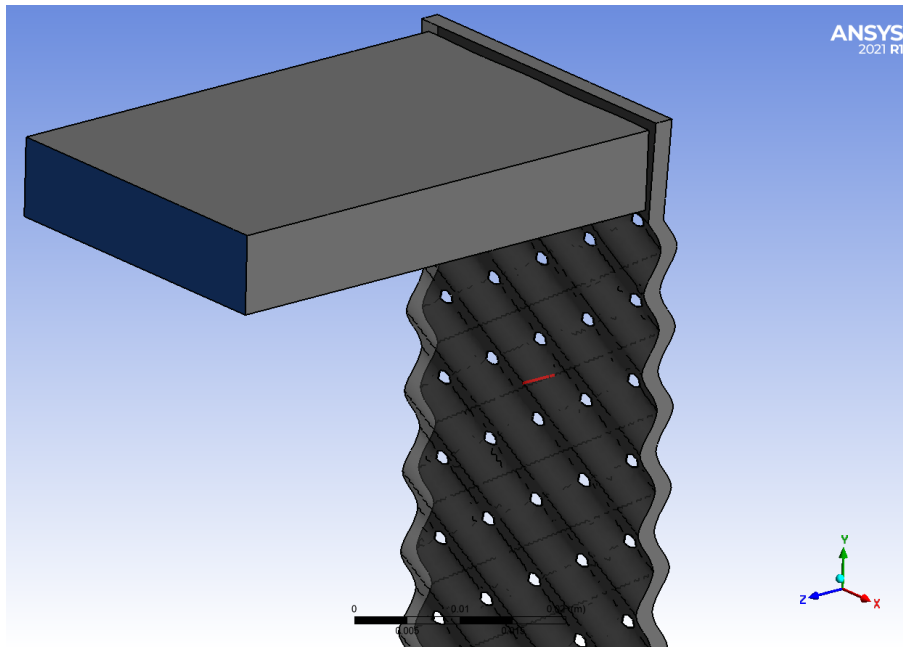

Figure 10: *Line probe showing position of velocity analysis.*

In each step, the cell size was decreased with approximately a factor of 1.5. The resulting meshes were run for Re 2000 and Re 5000. A rough estimation for the first layer thickness was performed according with section 2.8.2 resulting in a first layer thickness of 25µm. This resulted in a y^+ below 5 for both given Reynolds numbers. Three prismlayers were used with a growth rate of 1.2. The results are shown in table 2 & 3 below. Figures of the mesh within the channel can be seen in figure 11. For the finest mesh, fully converged results were not possible. These solutions were run for another 500 iterations and then averaged values were used.

Table 2: Grid convergence study, Re 2000		
Mesh size	Pressure drop [kPa]	$\Delta T[K]$
0.1M cells	12.0	25.25
0.45M cells	14.1	26.06
1.5M cells	13.7	26.38
2.8M cells	13.6	26.39
Table 3: Grid convergence study, Re 5000		
Mesh size	Pressure drop [kPa]	$\Delta T[K]$
0.1M cells	75.1	15.02
0.45M cells	89.5	15.25
1.5M cells	86.9	15.28
2.8M cells	85.4	15.27
11.7M cells	81.0	15.24
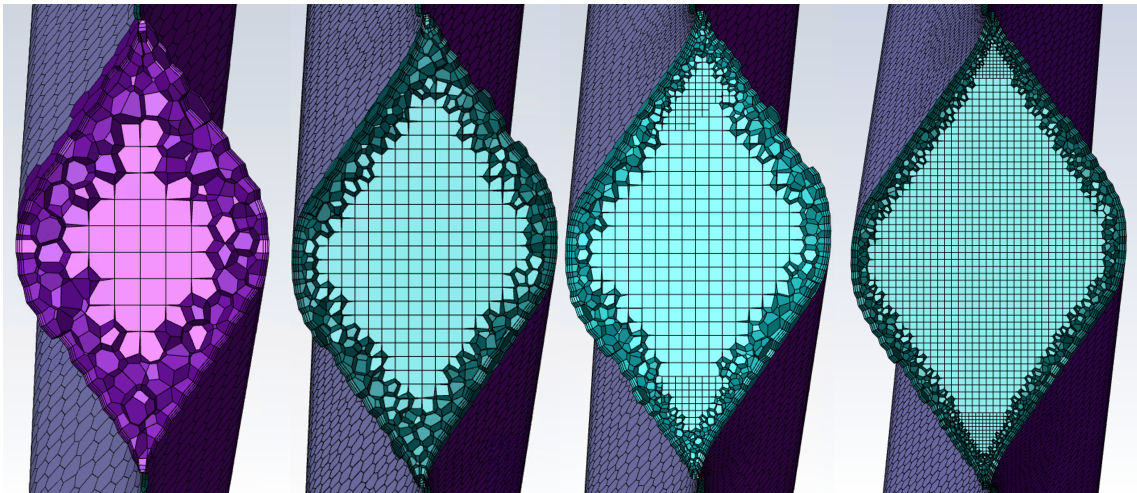
Figure 11: *The different meshes 0.45M cells (left) to 11.7M cells(right).*

Since there were barely any differences between the results for 1.5M cells and 2.8M cells, a suitable element size related to the 1.5M cell mesh was chosen and a sensitivity analysis was performed on the boundary layer. First, the number of boundary layers were analyzed to see how the result might change if the prismlayers faded more up into the freestream. These results are presented in table 4 and figure 12 where a constant growth rate of 1.2 was used.

31

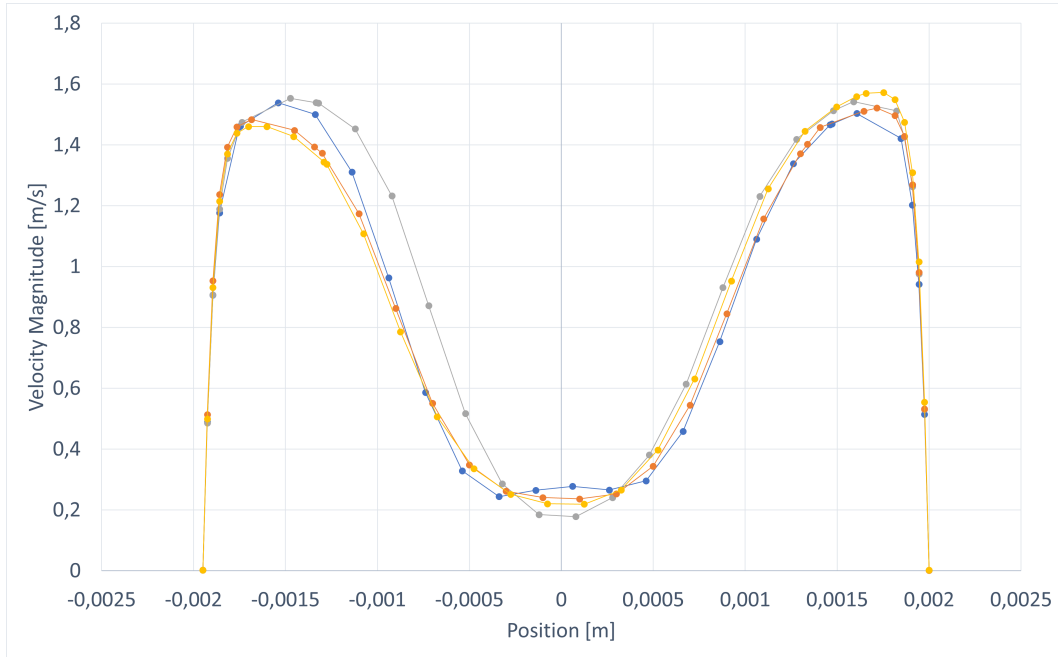| Table 4: Varying number of boundary layers, Re 2000			
Number of layers	Total Thickness [µm]	Pressure drop [kPa]	$\Delta T[K]$
3	43	13.7	26.40
4	52	13.8	26.52
5	62	13.8	26.54
6	75	13.7	26.60

Figure 12: *Velocity profile to different amounts of prism-layers.(3 Layers Blue, 4 Layers Grey, 5 Layers Orange, 6 Layers Yellow)*

For the given first layer thickness of 25µm a number of 5 layers seems to capture the gradients similarly to 6 layers. As seen in figure 12 both three and four layers does not seem sufficient looking at the left hand side of the picture. Regarding pressure drop and outlet temperature, no clear correlation can be seen. However the difference seems so be declining when increasing number of prism-layers. Therefore, when moving on to analysing the first layer thickness, the number of layers were varied to make sure the total thickness for the prism-layers were at least 62µm. The different setups are displayed in table 5 below.

Table 5: Setup definition for varied first layer thickness		
First layer thickness [µm]	Number of layers	Mesh size
10	10	2.6M cells
17.5	7	2.1M cells
25	5	1.8M cells
50	3	1.4M cells

The above setups were run for both Re 2000 and Re 5000 to understand how y^+ varies between them, this as the boundary layer gets thinner for higher Reynolds numbers. This was also performed to understand the sensitivity of the grid regarding heat transfer, since the approximation of wall shear stress directly affects this. The results are presented in table 6 & 7 below.

Table 6: First layer thickness analysis, Re 2000			
First layer thickness [µm]	Average y$^+$	$\Delta T[K]$	Pressure drop [kPa]
10	1.01	25.92	13.4
17.5	1.68	26.17	13.7
25	2.31	26.54	13.9
50	4.15	26.31	13.3

Table 7: First layer thickness analysis, Re 5000			
First layer thickness [µm]	Average y$^+$	$\Delta T[K]$	Pressure drop [kPa]
10	1.82	15.31	86.8
17.5	2.99	15.48	87.9
25	4.08	15.36	86.7
50	7.31	14.77	85.8

A first layer thickness of 25µm was chosen due to the fact that it gives reasonable y^+ values below 5 for both Re 2000 and Re 5000. It can also be seen that the outlet temperature is off for $y^+ > 5$. Plots showing velocity profiles are displayed in figure 14.
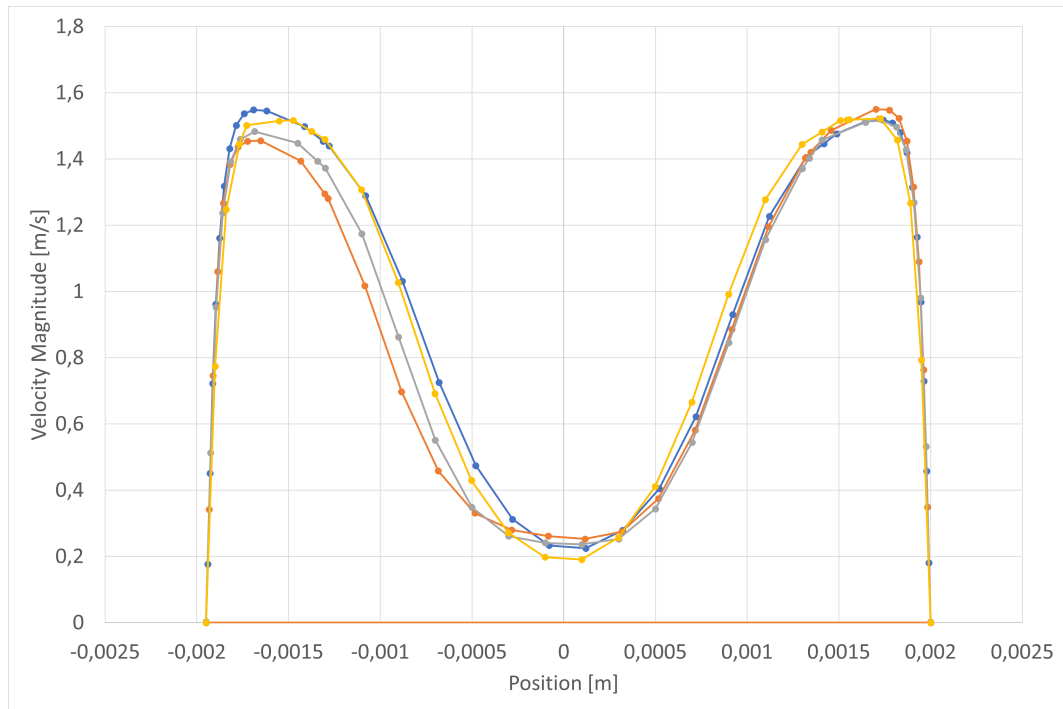
Figure 13: *Velocity profile to different first layer thicknesses, for Re=2000.*
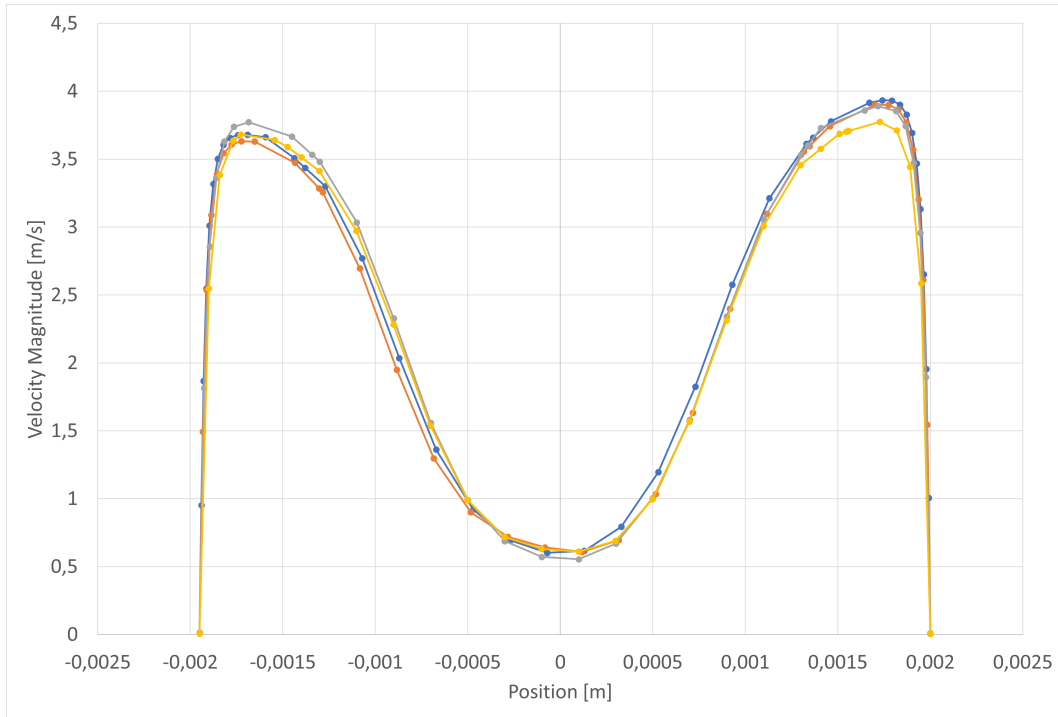
Figure 14: *Velocity profile to different first layer thicknesses, for Re=5000.*

Taking both results from table 5 & 6 into account, aswell as figure 14 and computational capacity. It was decided that the final mesh will use a first layer thickness of 25 with a number of 5 prismlayers. The final mesh contains 1.8M cells and will be used for the future simulations in this report regarding the small test plate. Later, this mesh will be scaled to fit the commercial plate, in accordance with Reynolds similarity principle discussed in section 2.4.

5.2   Initial parameter study

5.2.1   Global Parameters

Since the commercial plate is much larger than the test plate, an initial study on the parameters will be run on the test plate to rule out those with negligible affect. Also local phenomenon can be studied on the small test plate due to an ongoing PhD project on wall modelled LES simulations. However, there is no test rig for this plate yet, hence no experimental data is available at the moment. For the commercial plate, experimental data is available and can be utilized for global quantities such as pressure drop and outlet temperature.

With the chosen mesh from the mesh convergence study a default case was run with all parameters set to their default values. In Table 8, some values for the GEKO model are compared to the standard turbulence models for Re 1600.

Table 8: GEKO comparison		
	Re 1600	
Model	ΔP	kA
GEKO-1.75	-	-
GEKO-2.5	-3.3%	1.4%
GEKO-0.7	19.5%	2.9%
k-omega SST	-9.2%	0.8%
Standard k-epsilon	16.3%	-0.9%

Here it can be seen that the default GEKO-1.75 settings does not match well with the k-omega SST model as expected. The pressure drop is significantly lower for this model, even compared to GEKO-2.5. However when comparing with the standard k-epsilon model, the results are more expected as GEKO-1.0 should be similar in characteristics to the Standard k-epsilon model, similar results can be seen for GEKO-0.7.

Thereafter all parameters were tested for their extreme values, making sure to only vary one variable at a time. The results are presented in table 9 below. At this stage, simulations were run for Re 2000 and Re 5000 as well. The relation found is that with an increased Reynolds number, the relative differences increases as well.

Table 9: Extreme values for the GEKO model parameters						
	Re 1600		Re 2000		Re 5000	
Model	ΔP	kA	ΔP	kA	ΔP	kA
GEKO-1.75	-	-	-	-	-	-
GEKO-2.5	-3.3%	1.4%	-6.5%	1.3%	-9.7%	-0.1%
GEKO-0.7	19.5%	2.9%	24.7%	3.7%	27.6%	2.9%
GEKO:($C_{NW} = 2$)	0.9%	-0.5%	3.4%	0.3%	5.0%	1.0%
GEKO:($C_{NW} = -2$)	-2.1%	0.7%	-6.0%	0.3%	-9.5%	-0.9%
GEKO:($C_{JET} = 1$)	-	-	-0.4%	-0.1%	0.0%	0.0%
GEKO:($C_{JET} = 0$)	-	-	0.1%	-0.0%	0.1%	0.0%
GEKO:($C_{MIX} = 0.5$)	-	-	-0.1%	0.0%	0.1%	0.0%
GEKO:($C_{MIX} = 1$)	-	-	0.3%	0.1%	0.3%	0.1%
GEKO:($C_{CORNER} = 1.5$)	-8.8%	2.3%	-7.3%	0.9%	-7.9%	0.4%
GEKO:($C_{CURV} = 1.5$)	0.5%	0.0%	-2.8%	0.1%	-3.6%	0.0%

Parameters with most influence on the results based on the generated output parameters are: $C_{SEP}, C_{NW}, C_{CORNER}$ and C_{CURV}. However, it has not been taken into consideration that parameters may have more effect with increased or decreased C_{SEP}. Different combinations of these parameters were run in order to understand how they vary depending on what value on C_{SEP} was set, see table 10. Other combinations were tested for parameters excluded but showed no difference from previous observations. Some combinations were conducted for all Reynolds numbers but only the Re 1600 case is shown since it will be compared to local phenomenons later on.

Table 10: Combinations of $C_{SEP}, C_{NW}, C_{CORNER}$ and C_{CURV}, Re 1600		
Model	ΔP	kA
GEKO-1.75	0.0%	0.00%
GEKO-2.5	-3.3%	1.4%
GEKO-0.7	19.5%	2.9%
GEKO:(CSEP=2.5, CNW=2)	-2.5%	1.2%
GEKO:(CSEP=2.5, CNW=-2)	-4.4%	1.8%
GEKO:(CSEP=0.7, CNW=2)	28.5%	4.2%
GEKO:(CSEP=0.7, CNW=-2)	2.8%	1.4%
GEKO:(CSEP=0.7, CCORNER=1.5)	11.5%	4.1%
GEKO:(CSEP=0.7, CCURV=1.5)	20.7%	3.1%
GEKO:(CSEP=0.7, CNW=2, CCORNER=1.5)	18.3%	5.1%
GEKO:(CSEP=0.7, CNW=-2, CCORNER=1.5)	-0.9%	3.5%

When comparing these simulations, it can be seen that as C_{SEP} is increased, C_{NW} barely has any impact on pressure drop or heat transfer. However, for lower C_{SEP}, C_{NW} has a stronger impact on especially pressure drop, however, not that much on heat transfer.

Regarding C_{CORNER} in combination with lower C_{SEP}, it can directly be seen that it still has approximately the same effect as it did with C_{SEP} set to default. The impact of C_{CORNER} seems to increase with increased C_{NW}.

C_{CURV} barely has any impact on either pressure drop or heat transfer and will therefore not be prioritized when moving on to the commercial plate. However this could be because of the low Reynolds Number correlated to table 7, as it can be seen that increased Reynolds number did in fact have more impact on results.

5.2.2 Local Phenomena

An ongoing PhD project, run by Gustav Karlsson, has been run before and in parallel to this thesis project where well refined Wall-modeled LES (WM LES) simulations has been performed. Data from this projectwas kindly sent over and has been extracted and used for analysing local phenomenons in the geometry. The same line probes used in the mesh-study, figure 10, has been utilised and results are presented below. All velocity

38

profiles are presented component wise as the model yields different results in different directions. Based on the previous section, mainly parameters with more impact will be further analysed in this section.
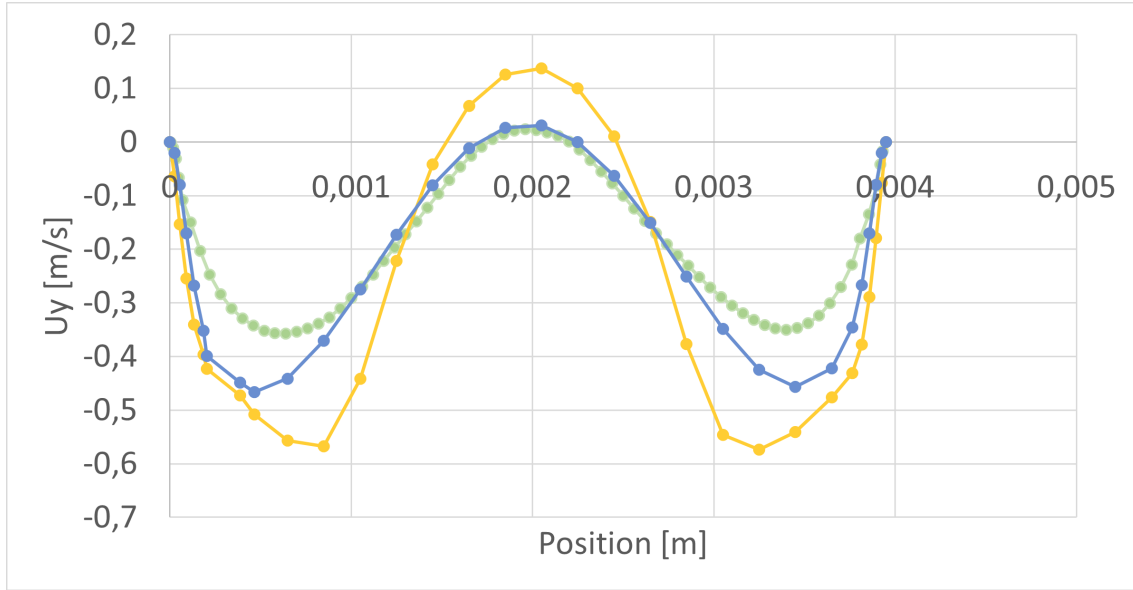

Figure 15: *Velocity probe of RANS models to WM LES. (Green: Wall modeled LES, Yellow: k-omega SST, Blue: Standard k-epsilon)*

Figure 15 shows the y-component for the velocity-profile of the standard turbulence models in relation to the WM LES. It can clearly be seen that the velocities are significantly over and undershooting for the k-omega SST model. The standard k-epsilon model seems to give an good approximation for the middle part of the channel and the re-circulation region but still undershoots for the near wall gradients.

Other quantities were also extracted such as eddy viscosity and turbulent kinetic energy but are only compared to the standard turbulence models for reference data. In figure 16, it can be seen that the model acts as expected.
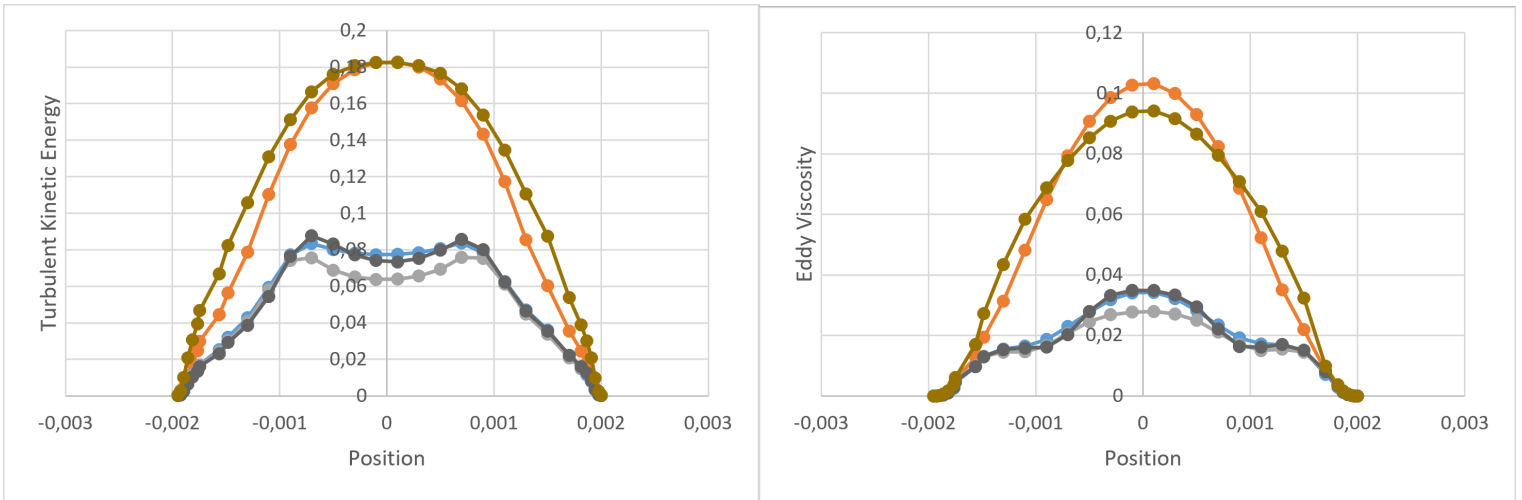
Figure 16: *C_{SEP} plotted in comparison to standard RANS models for turbulence quantities. (Blue: GEKO-1.75, Orange: GEKO-0.7, Grey: GEKO-2.5, black: k-omega SST, Brown: Standard k-epsilon)*
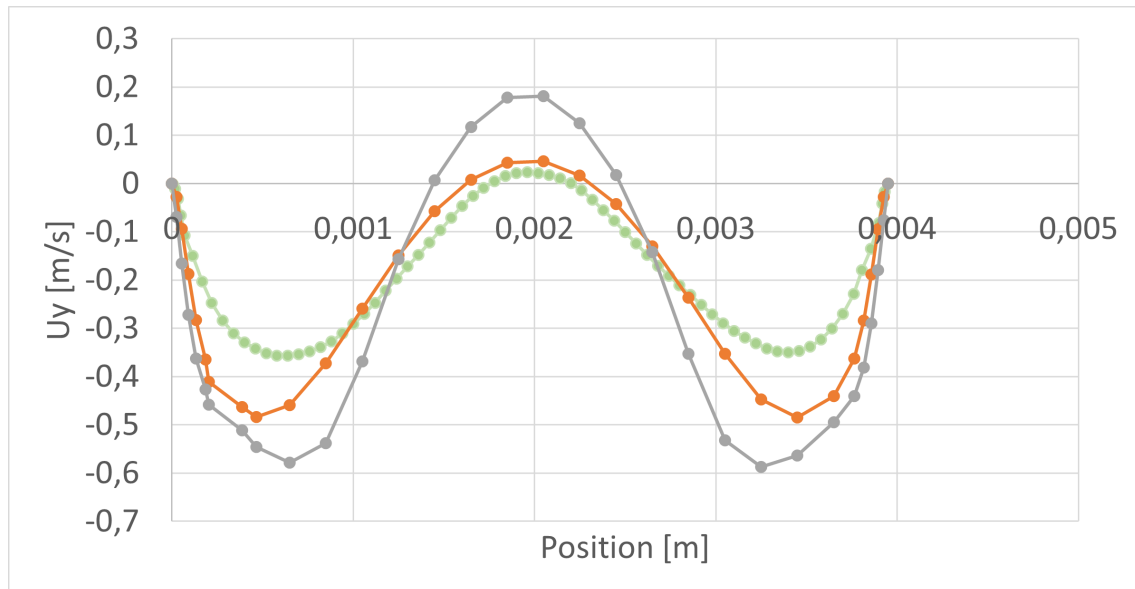

Figure 17: *Varying C_{SEP} in comparison to WM LES. (Green: Wall modeled LES, Orange: GEKO-0.7, Grey: GEKO-2.5)*

In figure 17 GEKO-0.7 and GEKO-2.5 is displayed compared to WM LES. Similar behaviour can be seen compared to figure 15 where a higher CSEP is comparable to the K-Omega SST model and a low CSEP is more similar to the K-epsilon model. It can also be seen that a lower CSEP seems be yielding closer results to the WM LES. Also

when plotting the x- and z-component similar behaviour is seen for varying CSEP, see
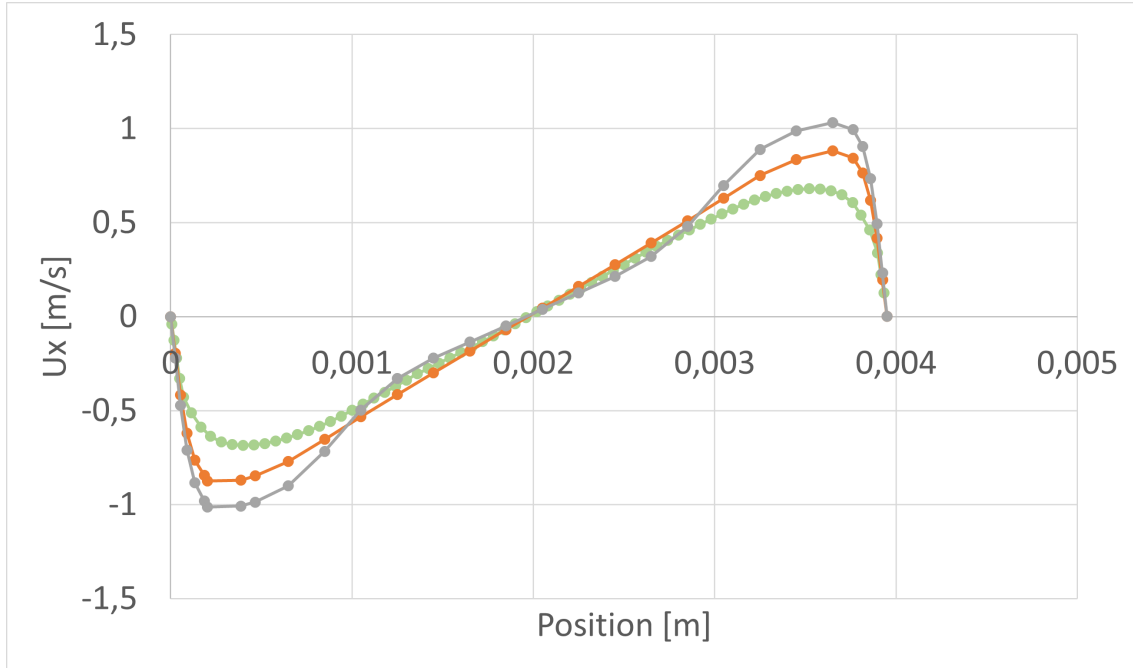figure 18 & figure 19

Figure 18: *Varying C_{SEP} in comparison to WM LES. (Green: Wall modeled LES, Orange: GEKO-0.7, Grey: GEKO-2.5)*
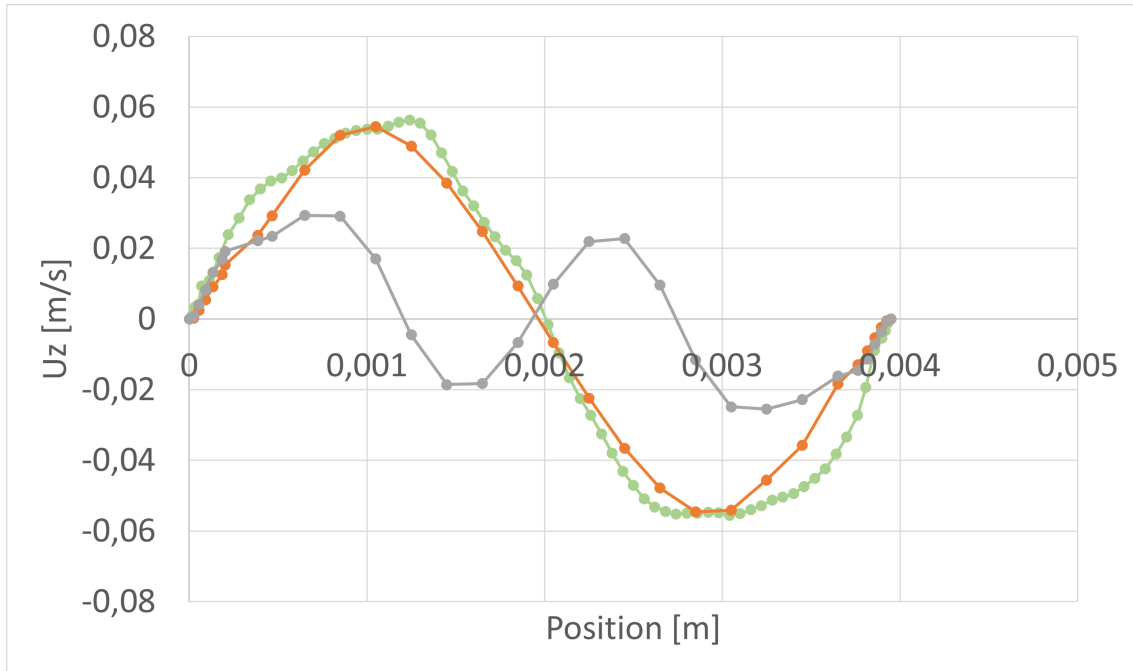
Figure 19: *Varying C_{SEP} in comparison to WM LES. (Green: Wall modeled LES, Orange: GEKO-0.7, Grey: GEKO-2.5)*

Next up, C_{NW} was analyzed in combination with $C_{SEP} = 0.7$. The results are shown in figure 20.
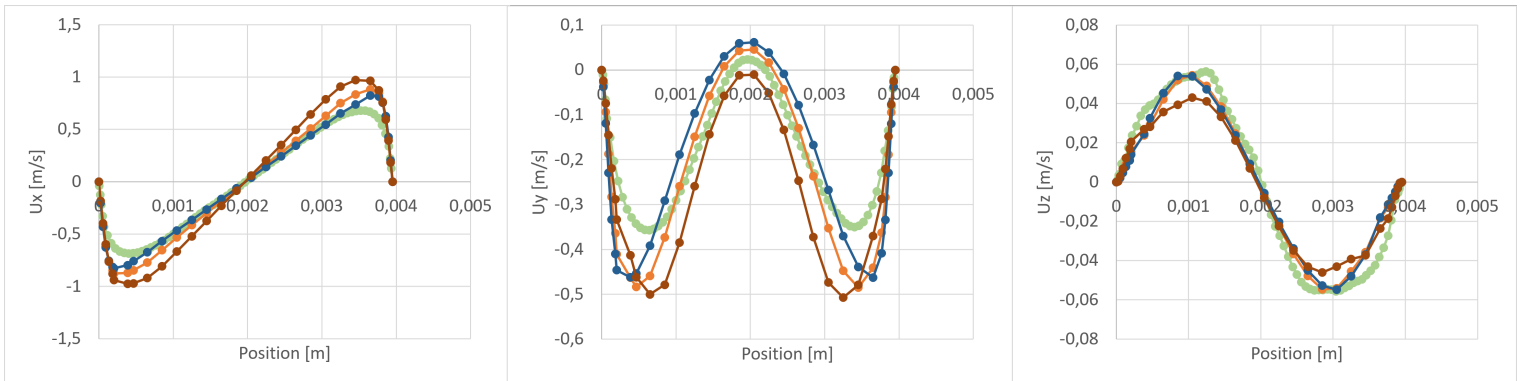

Figure 20: *Varying C_{NW} in comparison to WM LES. (Green: Wall modeled LES, Orange: GEKO-0.7, Blue: GEKO:(C_{SEP}=0.7,C_{NW}=2), Brown: GEKO:(C_{SEP}=0.7,C_{NW}=-2))*

It can be seen that for a low C_{NW}, the velocity profiles deviate more than for the standard values. For a high C_{NW} the x-component becomes more accurate compared to

42

the WM LES, however, the y-component seems to overshoot. For the z-component, no improvement was made with increased C_{NW}, however lower C_{NW} gives worse results.

Both C_{CORNER} and C_{CURV} was also plotted, results for C_{CORNER} can be seen in figure 21. Since no differences was observed for C_{CURV}, results are not included in this report. It seems like C_{CORNER} generates strange results for both the x- and y-component while the z-component is greatly improved. The improvement can be explained by the added nonlinear terms effect increase with low velocities, but overall C_{CORNER} doesn't seem to yield more accurate results.
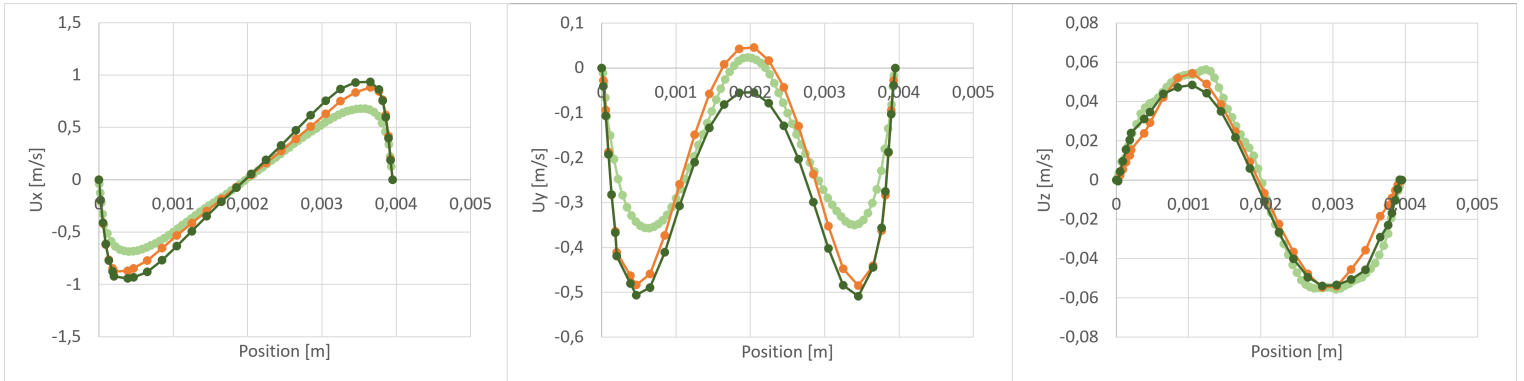

Figure 21: C_{CORNER} *plotted in comparison to WM LES.(Light Green: Wall modeled LES, Dark Green: GEKO:(C_{SEP}=0.7,C_{CORNER}=1.5), Orange: GEKO-0.7)*

5.3 Parameter study on commercial plate

From the earlier parameter study in section 5.2, parameters with most significance on the overall results were mainly C_{SEP} and C_{NW}. The best predicted fit to the WM LES were then GEKO:($C_{SEP} = 0.7$, $C_{NW} = 2.0$) whichs' combination will be tested for the bigger plate. In addition, GEKO-1.75 and GEKO-0.7 were also run.

The bigger plates comes in many different configurations with both high, low and mix-theta chevron patterns. The same simulations will be run on all these since no reference data is available. For each GEKO model, three different pressure drops of 25, 50 and 100kPa were run to see differences for varying Reynolds numbers. Reference simulations for the traditional turbulence models Standard k-epsilon and k-omega SST are also run for the 25kPa pressure drop. Results are shown in table 11 below and shows deviation from experimental results.

Table 11: GEKO models in comparison to experimental values for High Theta pattern.						
Model	25kPa		50kPa		100kPa	
High Theta Pattern	ΔP	kA	ΔP	kA	ΔP	kA
k-omega SST	-27.0%	-9.7%	-	-	-	-
Standard K-epsilon	-11.7%	-21.0%	-	-	-	-
GEKO-1.75	-26.1%	-10.6%	-27.7%	-10.0%	-29.4%	-9.3%
GEKO-0.7	-0.6%	-9.8%	-1.4%	-6.8%	-2.6%	-3.8%
GEKO:($C_{SEP} = 0.7, C_{NW} = 2$)	11.2%	-7.0%	10.6%	-2.9%	9.6%	1.4%
Low Theta Pattern	ΔP	kA	ΔP	kA	ΔP	kA
k-omega SST	-13.4%	-1.7%	-	-	-	-
Standard K-epsilon	-14.4%	-5.9%	-	-	-	-
GEKO-1.75	-13.8%	-0.7%	-12.6%	0.2%	-11.9%	-1.3%
GEKO-0.7	-13.4%	1.3%	-11.8%	2.1%	-12.4%	1.5%
GEKO:($C_{SEP} = 0.7, C_{NW} = 2$)	-12.1%	1.5%	-10.4%	3.5%	-10.5%	3.8%
Mix Theta Pattern	ΔP	kA	ΔP	kA	ΔP	kA
k-omega SST	-25.1%	-10.5%	-	-	-	-
Standard K-epsilon	-21.0%	-17.9%	-	-	-	-
GEKO-1.75	-27.5%	-11.0%	-30.5%	-10.9%	-34.3%	10.8%
GEKO-0.7	-12.4%	-7.9%	-14.6%	-6.1%	-18.0%	-6.5%
GEKO:($C_{SEP} = 0.7, C_{NW} = 2$)	-4.8%	-4.8%	-7.5%	-3.0%	-11.0%	-1.5%

Here it can be seen that for the high theta pattern, GEKO:($C_{SEP} = 0.7$ $C_{NW} = 2.0$)

44

does not generate the closest results when observing the global parameters as expected from the initial parameter-study in section 5.2. Since the initial parameter-study used a high theta pattern, it was expected to yield similar results for the same pattern. Instead, for the high-theta pattern it seems to be more accurate with GEKO-0.7 when observing the global parameters. For this channel, a slightly lower C_{SEP} in combination with a high C_{NW} would most likely generate better results.

For the low theta pattern, changing C_{SEP} barely made any difference on the results. Also for GEKO:($C_{SEP} = 0.7$, $C_{NW} = 2.0$) where the high theta overestimates pressure drop, the low theta pattern is underestimated. It should be noted though that the heat transfer is more accurate for the low theta pattern than for both mix and high theta.

For the mix theta pattern, GEKO:($C_{SEP} = 0.7$, $C_{NW} = 2.0$) came the closest to experimental values for pressure drop and heat transfer then the other model versions. As expected, all results for the mix theta pattern falls between high- and low-theta as it is a combination of these two.

Some general observations regarding the parameters C_{SEP} and C_{NW} is that they still behave in similar ways as for the small test-plate. When decreasing C_{SEP}, both pressure drop and heat transfer increases. When increasing C_{NW} both pressure drop and heat transfer increases. This is expected from the literature and from earlier simulations.

When comparing the GEKO-models to the traditional k-omega SST and standard k-epsilon model, it can be seen that the GEKO-models generate better results for all the channels, both in regards to pressure drop and heat transfer.

6   Conclusion & Future Work

The purpose of this thesis was to study the new GEKO-model and calibrate it for a commercial plate heat exchanger to see if better results can be achieved for predicting pressure drop and heat transfer.

In short, the thesis has shown that indeed better results could be achieved by adjusting the model parameters C_{SEP} and C_{NW} when comparing to more traditional turbulence models. Proposed parameter combinations vary depending on the channels and plate combinations but could be for a high theta channel GEKO-0.7 and for a mix theta channel GEKO:($C_{SEP} = 0.7$, $C_{NW} = 2.0$). It could also be noted that in order to generate better results in terms of heat transfer for the high theta pattern, a slightly higher value for C_{SEP} could be chosen in combination with a higher C_{NW}.

The low theta pattern seemed to be unaffected by the model parameter choices made. This is still unexplained and has not been further touched upon in this project. In parallel to this thesis, multiple other projects have taken place and mainly two suggestions for affecting the low-theta channel has been discussed. The first is including ports in the simulations and the second one is to use a non-isotropic turbulence model. None of these have been further studied but could be further worked upon.

The parameters have also been tested and compared with a high-resolved LES-study from a parallel PhD project on a smaller test-plate, implying that the choice of parameter values yields the closest correlation with local velocity-profiles studied. This test-plate does however not exist in real life, and therefore it would be beneficial to in the future, make a high resolved LES simulation for a plate that have experimental test-results. This could then be used as a baseline to further study the physics within the heat exchanger and understand more detailed how the local phenomenons correlate with the global parameters.

Finally, another important aspect of this work is that this was only conducted for one commercial heat exchanger. The GEKO-model should be more intensively tested on other plate heat exchanger models and further validated before potentially switching to use this more frequently.

References

[1] Alfa Laval AB/ Bysted AB. Annual Report 2020 Preserving solar energy to brighten gloomy days. URL: https://www.alfalaval.com/globalassets/documents/investors/english/annual-reports/annual-report-2020x.pdf. (accessed: 01.20.2022).

[2] CFD-Online. Turbulence free-stream boundary conditions. URL: https://www.cfd-online.com/Wiki/Turbulence_free-stream_boundary_conditions. (accessed: 03.23.2022).

[3] Nick Connor. What is Logarithmic Mean Temperature Difference – LMTD – Definition. URL: https://www.thermal-engineering.org/what-is-logarithmic-mean-temperature-difference-lmtd-definition/. (accessed: 12.20.2021).

[4] A. Matsyushenko NTS St. Petersburg F.R. Menter R. Lechner ANSYS German GmbH. "Best Practice: Generalized k-ω Two-Equation Turbulence Model in ANSYS CFD (GEKO)". In: ANSYS Technical Report 1.00 (Jan. 2019).

[5] ANSYS Inc. "ANSYS Fluent Theory Guide". In: Release: 15.0 (Nov. 2013).

[6] Alfa Laval. Alfa Laval in brief – who we are and what we do. URL: https://www.alfalaval.com/about-us/our-company. (accessed: 10.30.2021).

[7] Alfa Laval. Packningsförsedda plattvärmeväxlare. URL: https://www.alfalaval.se/produkter/varmeoverforing/plattvarmevaxlare/packningsforsedda-plattvarmevaxlare/. (accessed: 12.20.2021).

[8] Alfa Laval. Plate heat exchanger calculation method. URL: https://www.alfalaval.se/microsites/packningsforsedda-plattvarmevaxlare/verktyg/berakningsmetod/. (accessed: 12.15.2021).

[9] Alfa Laval. Plate Technology. URL: https://www.alfalaval.se/microsites/packningsforsedda-plattvarmevaxlare/verktyg/platt-teknik/. (accessed: 12.15.2021).

[10] Stephen B. Pope. Turbulent Flows. Cambridge University Press, 2000. ISBN: 0521598869.

[11] Sim Scale. Wall Boundary Condition. URL: https://www.simscale.com/docs/simulation-setup/boundary-conditions/wall/. (accessed: 01.30.2022).

[12] H K Versteeg and W. Malalasekera. An Introduction to Computational Fluid Dynamics. THE FINITE 2nd ed. Harlow: Pearson Education Limited, 2007. ISBN: 978-0-13-127498-3.

[13]   Yoshihisa Yamamoto. <u>Fundamentals of Noise Processes</u>. Cambridge University Press, 2017. ISBN: 052181748X.